



Publication Year	2016
Acceptance in OA @INAF	2020-06-23T16:50:56Z
Title	Present-day aeolian activity in Herschel Crater, Mars
Authors	CARDINALE, MARCO; Silvestro, Simone; Vaz, David A.; Michaels, Timothy; Bourke, Mary C.; et al.
DOI	10.1016/j.icarus.2015.10.022
Handle	http://hdl.handle.net/20.500.12386/26202
Journal	ICARUS
Number	265

Manuscript Number:

Title: Present-Day Aeolian Activity in Herschel Crater, Mars.

Article Type: Regular Article

Keywords: Sand transport; Dunes; Ripples, Aeolian Processes; Herschel Crater.

Corresponding Author: Dr. Marco Cardinale, Ph.D.

Corresponding Author's Institution: Università degli Studi G.d'Annunzio

First Author: Marco Cardinale, Ph.D.

Order of Authors: Marco Cardinale, Ph.D.; Simone Silvestro, Ph.D; David A. Vaz, Ph.D; Timothy Michaels, Ph.D; Goro Komatsu, Ph.D; Mary Bourke, Prof.; Lucia Marinangeli, Prof.

Abstract: In this report, we show evidence for ripple and dune migration in Herschel Crater on Mars. We estimate an average dune migration of 0.8 meters and a minimum ripple migration of 1.1 meters in a time span of 3.7 Earth-Years.

These dunes and ripples are mainly shaped by prevailing winds coming from the north, however we also report the presence of secondary winds enhanced by the crater rim at regional scale and deflected by the dune topography at the dune scale.

These last are predicted by the Mars Regional Atmospheric Modeling System (MRAMS), an atmospheric mesoscale model, while the dominant flows from the north are underestimated.

Modeled winds at the local scale refer that a multi directional wind regime is indicated as the first cause of the diverse set of ripples overlapping one on other.

For the first time, a survey integrating the assessment of dune and ripple migration is presented, showing how dune topography can influence the migration patterns of ripples and how underlying regional topography seems to control the rates of dune migration.

The migration patterns suggest that the prevailing winds from the north are locally-deflected winds (blowing from the NNW and from the NNE before deflection).

Suggested Reviewers: Matthew Choinacki
chojan1@pirl.lpl.arizona.edu

Candice Hansen
cjhansen@psi.edu

Robert A. Craddock
craddockb@si.edu

Rosalyn K. Hayward
rhayward@usgs.gov

Paul Geissler
pgeissler@usgs.gov

Opposed Reviewers:

Editor
Editorial office of Icarus

May 08th, 2015

Dear Editor, We are submitting a manuscript entitled "Present-day aeolian activity in Herschel Crater, Mars." prepared by M. Cardinale et al. to this journal
We would like to submit the manuscript only for the Online version and we would like to make colour choices for article's 11 figures as follows:

Online version

Colour: Figure 1, Figure 2, Figure 3, Figure 4, Figure 6, Figure 8, Figure 9, Figure 10, Figure 11, Figure 12.

B/W: Figure 5, Figure 7, Table 1, Table 2.

Sincerely yours,

A handwritten signature in black ink, reading "Marco Cardinale". The script is fluid and cursive, with the first name "Marco" and last name "Cardinale" clearly distinguishable.

Marco Cardinale
Dipartimento di Scienze
Psicologiche della Salute e del Territorio
Universita' d'Annunzio
Via dei Vestini 31.
66013 Chieti, Italy
Phone: +39 – 0871- 3555331.
email: marco.cardinale@unich.it

Present-day aeolian activity in Herschel Crater, Mars.

Marco Cardinale¹, Simone Silvestro^{2,3}, David A. Vaz^{4,5}, Timothy Michaels³, Goro Komatsu⁶,
Mary C. Bourke⁷, Lucia Marinangeli¹,

¹Dipartimento di Scienze Psicologiche della Salute e della Terra, Università G. d' Annunzio
Via dei Vestini 31, 66013 Chieti Scalo, Italy

²INAF, Osservatorio Astronomico di Capodimonte,
Salita Moiarriello 16, Napoli, Italy.

³Carl Sagan Center, SETI Institute
189 N. Bernardo Avenue, Suite 100 Mountain View, CA
94043, USA

⁴Centre for Earth and Space Research of the University of Coimbra,
Observatório Astronómico da Universidade de Coimbra,
Almas de Freire, 3040-004 Coimbra, Portugal.

⁵CERENA, Instituto Superior Técnico,
Av. Rovisco Pais, 1049-001 Lisboa, Portugal.

⁶International Research School of Planetary Sciences
Università G. d' Annunzio
Viale Pindaro, 42
65127 Pescara, Italy.

⁷Department of Geography, Trinity College Dublin,
Dublin, Ireland.

Submitted to Icarus

08 05, 2015

17 pages including text and captions

- 12 figures

2 tables

Corresponding author: Marco Cardinale
Dipartimento di Scienze Psicologiche Umanistiche e della Terra, Università d'Annunzio
Via dei Vestini 31, 66013 Chieti Scalo, Italy
Phone: +39-0871-355-5331
email: marco.cardinale@unich.it

Proposed running Title:
Aeolian activity in Herschel Crater (Mars).

Abstract

In this report, we show evidence for ripple and dune migration in Herschel Crater on Mars.

We estimate an average dune migration of 0.8 meters and a minimum ripple migration of 1.1 meters in a time span of 3.7 Earth-Years.

These dunes and ripples are mainly shaped by prevailing winds coming from the north, however we also report the presence of secondary winds enhanced by the crater rim at regional scale and deflected by the dune topography at the dune scale.

These last are predicted by the Mars Regional Atmospheric Modeling System (MRAMS), an atmospheric mesoscale model, while the dominant flows from the north are underestimated.

Modeled winds at the local scale refer that a multi directional wind regime is indicated as the first cause of the diverse set of ripples overlapping one on other.

For the first time, a survey integrating the assessment of dune and ripple migration is presented, showing how dune topography can influence the migration patterns of ripples and how underlying regional topography seems to control the rates of dune migration.

The migration patterns suggest that the prevailing winds from the north are locally-deflected winds (blowing from the NNW and from the NNE before deflection).

Keywords: Sand transport; Dunes; Ripples, Aeolian Processes; Herschel Crater.

71 **1. Introduction and study area**

72 The Martian surface has abundant active aeolian bedforms (Fenton, 2006; Bourke et al.,
73 2008) which have been recently observed to migrate in the current climatic setting (Silvestro et al.,
74 2010, 2011, 2013; Chojnacki et al., 2011; Hansen et al., 2011; Bridges et al., 2011, 2012, 2013;
75 Geissler et al., 2013; Sparavigna, 2013). New techniques that take advantage of the high resolution
76 of the HiRISE (High Resolution Imaging Science Experiment) data (McEwen et al., 2007) have
77 been recently applied to characterize small-scale aeolian bedforms on Mars. The migration rates of
78 ripples were computed using the Coregistration of Optically Sensed Images and Correlation (COSI-
79 Corr) software (Bridges et al., 2012), while ripple trends were automatically derived using the
80 Object-Based Ripple Analysis (OBRA) technique (Silvestro et al., 2011, 2013; Vaz and Silvestro,
81 2012, 2014).

82 The aim of this study is to use these two methods in combination to analyze dune and ripple
83 patterns and migration using a pair of overlapping HiRISE images in Herschel Crater, a 300 km
84 Noachian impact basin in the Mare Tyrrhenium region (MC22) (Figure 1). The dunes of Herschel are
85 of particular interest as they have been previously interpreted as ancient indurated aeolianites (due
86 to the grooved pattern visible on the dune slopes; Malin and Edgett, 2000). More recent images
87 from the HiRISE camera showed that such a pattern is formed by sand ripples which, together with
88 the dunes, are consistently migrating (Bridges et al., 2007, 2011, 2013;).

89 However, first evidences for sand motion in the Herschel Crater have been detected by (Cardinale et
90 al., 2012a).

91 In this work we compute ripple and dune migration rates and compare the migration
92 directions with the present-day winds simulated by the Mars Regional Atmospheric Modeling
93 System (MRAMS), a mesoscale atmospheric model (Michaels and Rafkin, 2008; Rafkin, 2001).

94 We use this wind model at two diverse grid scale to interpret the observed aeolian morphologies.

95 In this way, we test the capability of the wind model to predict the wind regime necessary for the
96 creation and the evolution of the Herschel dune fields; we show that the aeolian activity that is

shaping the dunes is not strictly unidirectional and that the topography of the crater is controlling the wind flow at the dune scale.

2. Methods

We conducted a detailed geomorphological analysis of dunes and ripples in Herschel Crater using a time series of HiRISE images and a stereo pair that was used to build a DTM with SOCET SET (Mattson et al., 2011) (Figure 1, Table 1). Images S1 and T3 (Table 1) were orthorectified over the DTM using the Co-registration of Optically Sensed Images and Correlation (COSI-Corr) software package (Leprince et al., 2007; Bridges et al., 2011). Dune morphometric parameters (slopes and aspect angles) were computed in ArcGIS and used to derive density stereoplots of the slipface surface vectors, providing an approximation to the main sediment flux direction (Figure 2d) (Silvestro et al., 2013). Ripple crestlines were mapped over the study dunes in the S1 image using the OBRA (Object-Based Ripple Analysis) procedure introduced by Vaz and Silvestro (2014). This technique is used to derive the main trends of the ripples, providing information about wind/sediment interactions at smaller scales (Figure 3).

The lee fronts of the dune slip faces were manually digitized on the S1 and T3 images in order to derive the dune migration rate and direction (Figure 4). In addition, we also evaluated the spatial distribution of the dune migration azimuth (Figure 5). We then used COSI-Corr to track the ripple displacement over the S1 and T3 images acquired 1359 Earth-days apart (Table 1). The result is a ripple displacement map (Figure 6) from which we derived the average ripple migration rate (Figures 7 and 8).

Finally, we estimated the potential timing of the sand-moving events by using the MRAMS mesoscale atmospheric model (Michaels and Rafkin, 2008; Rafkin et al., 2001) on two diverse grid scales. In the first one, the surface stress and wind direction have been modeled for one typical day for each of the four seasons (at $L_s = 210^\circ$ (southern summer), $L_s = 300^\circ$ (southern spring), $L_s = 30^\circ$ (southern winter) and $L_s = 120^\circ$ (southern autumn) at a spatial resolution of $\sim 8 \text{ km} \times 8 \text{ km}$ (Figure

123 9). The output model state was recorded every twenty Martian-minutes for four typical sols.
124 In the second atmospheric simulation, we used a model with ~2km grid spacing to constrain the
125 local wind conditions in the Herschel Crater (Fig.10). The modeled winds have been sorted into 24
126 equal width direction bins over the dune field and each point may have a maximum 24 vectors and
127 these ones show the downwind direction of the wind.
128 The instantaneous model was recorded for 12 seasons at $L_s=0^\circ$ (southern winter), $L_s=30^\circ$ (southern
129 winter), $L_s=60^\circ$ (winter), $L_s=90^\circ$ (northern winter), $L_s=120^\circ$ (southern autumn), $L_s=150^\circ$ (autumn),
130 $L_s=180^\circ$ (northern autumn), $L_s=210^\circ$ (southern summer), $L_s=240^\circ$ (summer), $L_s=270^\circ$ (northern
131 summer), $L_s=300^\circ$ (southern spring) and $L_s=330^\circ$ (spring) by the MRAMS (Fig.11).

132

133 **3. Dune and ripple morphology**

134 The study dunes are located in a ~1200 km² dune field in the western floor of Herschel
135 crater and consist of barchans and barchanoids (Cardinale et al., 2012b). These dunes can be more
136 than 60 m tall and spaced ~200-800 m apart. Some of the dunes present an asymmetric structure,
137 with the slip face being elongated obliquely (Figures 2b and c). Visual assessment and stereonet
138 analysis reveal a high dispersion in the dune slipface orientation and slope values clustering at ~30°
139 (Figure 2d). This reflects the concave shape of the barchan and barchanoid slipfaces. Most of the
140 slip face vectors are oriented toward the south, trending between ~60° and ~300° with a main mode
141 located at ~125° (Figure 2d), reflecting the dune slipface asymmetry.

142 In Figure 3 we show some examples of the different types of ripple patterns in the area. On
143 the dune flanks ripples are spaced 2-4 meters apart and are two-dimensional with typical “Y”
144 junction terminations (Figure 3a), while on the top of the dunes the ripple pattern is more three-
145 dimensional, with diverse ripple sets overlapping (Figure 3b). Such a ripple arrangement probably
146 reflects the coupling between ripple straightness and slope described by Rubin (2012) and observed
147 in the field by Howard (1977). The complexity of the ripple pattern is shown in the rose diagram in
148 Figure 3c (showing the distribution of the crestline trends mapped automatically over the dunes in

149 the yellow box). The overall length-weighted circular distribution of the mapped ripple traces shows
150 different trends and two main modes at $\sim 45^\circ$ and $\sim 135^\circ$.

151 **4. Bedform migration**

152 **4.1. Dunes**

153 In Figure 4a we show the areal distribution of the average dune migration vectors for 211
154 dunes computed by comparing the pair S1 and T3 (Table 1) ($\Delta t = 1359$ Earth-days). Dunes which do
155 not have a clear slipface are excluded from the analysis. The distribution of the lee motion is neither
156 uniform nor unidirectional. A higher migration value is reported for the dunes located in the
157 northern dune field sector (1.2-2.2 (m)) with the dune displacements decreasing toward the south
158 (Figure 4a). Such a N-S migration trend can be attributed to the abrupt change in the roughness at
159 the dune field margin which triggers the development of an internal boundary layer that thickens
160 downwind (Jerolmack et al., 2012). Figure 4b highlights the north-south migration trend (left) and
161 shows that the area with larger migration values (between -14.70° and -14.75° in latitude)
162 corresponds to a drop in elevation that is well represented in the northern part of the Herschel dune
163 field (right). This suggests that the underlying large-scale topography also contributes to the shape
164 of the internal boundary layer.

165 On average, the dunes migrated 0.8 meters toward the SSE (Figure 5a shows the computed
166 average vector) giving a rate of migration of 0.45 meter/Mars-year (MY) (~ 0.2 meter/Earth-year or
167 m/EY), assuming that this values is constant from year to year. The measurements show high
168 directional dispersion ($\mu = 162^\circ \pm 38^\circ$) (Figure 5b), which might be partially be due to the local
169 topography since the dunes are not migrating over a flat surface.

170 **4.2. Ripples**

171 In Figure 6 we show the ripple displacement map obtained with COSI-Corr. The map
172 reveals that significant movement occurred across the investigated area between March 2007 and
173 December 2010. In the northern area of the Herschel dune field the fastest ripples moved so far that
174 the correlation breaks down, that is, once the migration exceeds a distance at least equal to the

175 ripple wavelength (5.1 m) (Figure 6b). In the central and southern dune field sectors the ripple
176 displacement is smaller, so it can be traced (Figures 6a and c). The ripple migration rate also varies
177 with the height of the dunes, with the fastest migrating ripples located close to the dune crest of the
178 dunes (Figure 6c). This is the result of the linear relationship between height and ripple migration
179 also reported for the Nili Patera dunes (Bridges et al., 2012). During a period of 1359 Earth-days we
180 obtained an average vector for ripple migration of 1.1 meters and trending toward SSE (Figure 7a).
181 This gives a migration rate of 0.55 meters in one MY (~ 0.3 meters/EY). The measurements show a
182 high circular standard deviation (41.6°) and their directional trend is mainly bimodal with modes at
183 $\sim 175^\circ$ and $\sim 240^\circ$ (Figure 7b). The high directional dispersion of the ripple migration vectors is due
184 to the local dune topography which deflects the wind over the dunes as shown in Figure 8. In
185 particular, the secondary mode at $\sim 240^\circ$ is due to the ripple migration vectors in the lee of the dunes
186 (orange vectors in Figure 8).

187 **5. Modeled winds**

188 The atmospheric models (MRAMS simulations at 2 diverse grid scales) are used to valuate
189 wind strength and direction, to explain the observed aeolian morphologies and dune changes (
190 Fenton et al., 2005; Hayward et al., 2007; Chojnacki et al., 2011).

191 Due to the complex pattern of the Herschel dune field, we suppose a multi directional wind regime
192 to be estimated by these simulations.

193 In Figures 9a and 9b (wind model at 8 km grid space) we show the daily maximum MRAMS ratio
194 (stress / threshold stress) vectors over the whole dune field. We define the stress ratio as the
195 aerodynamic surface stress divided by the minimum threshold aerodynamic stress calculated using
196 the expressions of Greeley and Iversen (1985). Dominant modeled wind direction is from the west
197 to the east (Figure 9c) with the strongest winds blowing close to the western crater rim (Figure 9a).
198 The predicted stress values are just above the (Kok 2010) threshold for sand saltation maintenance
199 (10% of the Greeley and Iversen (1985) saltation initiation threshold). In Figure 9b we show the
200 modeled wind directional variability. A general trend is visible with the winds being more uni-

directional close to the western crater rim (see the lower circular STD in this area and Table 2). In Figure 9d we show the same data plotted by seasons with the important statistic parameters summarized in Table 2.

The strongest winds blow at $L_s=30^\circ$ (southern winter) from the west to the east with a circular STD of 34° . In the other seasons modeled winds are weaker and multi-directional ($CSTD>87^\circ$). Dominant winds from the north to the south, matching the dune and ripple migration direction, are not predicted by the model.

Output from MRAMS at 2km grid scale such as that of Fig. 10 is used to resolve topographically – influenced wind flows not explained in the previous wind simulation.

Modeled wind strength and direction from twelve Martian sols are examined here (Fig.11).

Within the investigated dune field a predominant wind distribution is not visible; a wind direction variability possibly induced by the crater topography is high in all the twelve studied seasons and the strongest modeled winds are predicted to blow from N-NE in spring ($L_s=330^\circ$).

The modeled winds by this second MRAMS simulation highlights that prevailing winds from north, matching the measured slip faces, are not predicted by this model.

According to this second simulation, we noticed that weaker winds are frequent in the Herschel Crater such as other areas previously studied (Silvestro et. al.2012, 2013).

Even in this second model, the simulated shear stress values are just above the Kok threshold for sand saltation maintenance with a maximum stress value of 0.30 for all the investigated seasons (Fig.12).

According to the recent numerical models on the Martian sand saltation, the hypothesis on the hysteresis phenomenon could show how after the initiation, the saltation can be sustained with weaker winds on martian surface (Kok, 2010).

227 6. Discussion and conclusion

228 Our results show that the ripples and the dunes in the Herschel Crater are mainly shaped by
229 winds blowing from the north to the south. However, the asymmetry in the dune form indicates that
230 the wind regime is not strictly uni-directional (Bourke M.C., 2009; Parteli et al., 2014).
231 In particular, following the model of Bagnold, (Bagnold, 1956), the influence of a local bimodal
232 wind regime (winds blowing from NNW and from NNE), should be the cause for the observed
233 asymmetry with the former probably being more frequent or stronger (Figure 2b-c).
234 The influence of more than one wind, the combination of dune collision, limb extension and
235 merging with downwind dunes (Bourke M.C., 2009) are also supported by the dunefield pattern
236 which is highly irregular and intricate (Bridges et al., 2007) and by the resultant bedform migration
237 directions.

238 The first MRAMS simulation, show modeled winds enhanced by the western crater rim
239 blowing to the east. The interaction of these flows with the dominant winds coming from the north
240 may be the cause of the observed dune morphology and migration direction. In the second MRAMS
241 simulation, the diverse combined wind flows may partially explain the intricate ripple pattern. The
242 ripple migration however, seems to be controlled by the local dune topography and any
243 extrapolation from local to dune field/regional scale has to be treated carefully.
244 The lack of dominant winds from the north in the MRAMS simulation can be attributed to the low
245 spatial and temporal coverage. A similar situation has also been reported by other workers
246 (Hayward et al., 2009; Silvestro et al., 2012) suggesting the importance of ground truth data when
247 deriving the wind regime of a certain area on Mars.

248 With the exception of the Nili Patera ripples, bedform migration rates in Herschel are
249 comparable to other areas on Mars (Bridges et al., 2012; Silvestro et al., 2011, 2013). However,
250 without continuous and long-term monitoring of Herschel and the other zones, this kind of
251 inference remains speculative.

252 In flat areas, changes in surface roughness can increase the boundary shear stress in the

253 upwind margins of dune fields (Jerolmack et al., 2012), producing spatial variations in the sediment
254 fluxes. In more complex terrains, like in the floor of Herschel crater, the observed relationship
255 between dune celerity and local topography (in particular the abrupt change in the roughness of
256 ~1km illustrated in the Fig.4) suggests that in addition to the roughness of the aeolian pattern, the
257 variations in the long wavelength topography (Pelletier et al., 2014) control the Herschel dunefield
258 properties.

259 Collectively, the combination of different methods of investigation helped to better decipher
260 the wind regime in Herschel Crater. At the dune field scale, the main winds from the north combine
261 with wind from the west enhanced by the western crater rim (the dune field is distant 28 km from
262 the westerly crater rim). At the dune scale, the topography of the dunes and the substrate
263 topography are controlling dune height, bedform migration rates and directions as described for the
264 White Sand dune field in New Mexico by Pelletier et al., 2014. The topography at regional and
265 local scale is indeed an important boundary condition that needs to be carefully addressed in order
266 to extract the best wind information from remote sensing images.

267

268 **Acknowledgements**

269 M. Cardinale is supported by a grant from the ASI (Agenzia Spaziale Italiana).

270

271

272 **References**

273

274 Bagnold, R.A. 1941. The physics of blown sand and desert dunes. London: Methuen, 265 pp.

275 Bourke, M.C. 2009. Barchan dune asymmetry: Observations from Mars and Earth. 2010 Icarus 205
276 (2010) , 183-197. DOI: 10.1016/j.icarus.2009.08.023.

277 Bourke, M.C., Edgett, K.S., Cantor, B.A. 2008. Recent Aeolian dune change on Mars. Geomorph 94,
278 247–255. <http://dx.doi.org/10.1016/j.geomorph.2007.05.012>.

279 Bridges, N.T., P. E. Geissler, A.S. McEwen, B.J. Thomson, F.C. Chuang, K. E. Herkenhoff, L.P.
 280 Keszthelyi, and S. Martínez-Alonso. 2007. Windy Mars: A dynamic planet as seen by the
 281 HiRISE camera, *Geophys. Res. Lett.*, 34, L23205, doi:10.1029/2007GL031445.

282 Bridges, N.T., Bourke, M.C., Geissler, P.E., Banks, M.E., Colon, C., Diniega, S., Golombek, M.P.,
 283 Hansen, C.J., Mattson S., McEwen A.S., Mellon, M.T., Stantzos N., and Thomson B.J. 2011.
 284 Planet-wide sand motion on Mars. *Geology*, January 2012, v.40, p. 31-34, first published on
 285 November 14, 2011, doi:10.1130/G32373.1.

286 Bridges, N. T., Ayoub F., Avouac J.P., Leprince S., Lucas A., Mattson S. 2012. Earth-like sand
 287 fluxes on Mars. *Nature*. 2012 May 9;485(7398):339-42. doi:10.1038/nature11022.

288 Bridges, N., Geissler, P.E., Silvestro, S and M. Banks. 2013. Bedform Migration on Mars: Current
 289 Results and Future Plans, *Aeolian Research*. <http://dx.doi.org/10.1016/j.aeolia.2013.02.004>.

290 Cardinale, M.; Silvestro, S.; Komatsu, G.; Vaz, D.A.; Michaels, T.I. 2012a. Evidences for Sand
 291 Motion in the Equatorial Region of Mars. 43rd Lunar and Planetary Science Conference, 2012
 292 LPI Contribution No. 1659, id.2452.

293 Cardinale, M., Komatsu, G., Silvestro, S. and Tirsch, D. 2012b. The influence of local topography
 294 for wind direction on Mars: two examples of dune fields in crater basins. *Earth Surf. Process.*
 295 *Landforms*, 37: 1437–1443. doi: 10.1002/esp.3289.

296 Chojnacki M., Burr D.M., Moersch J.E., Michaels T.I. 2011. Orbital observations of contemporary
 297 dune activity in Endeavour Crater, Meridiani Planum, Mars. *Journal of Geophysical Research*
 298 116: E00F19, doi:10.1029/2010JE003675.

299 Fenton, L. K. 2006. Dune migration and slip face advancement in the Rabe Crater dune field, Mars,
 300 *Geophys. Res. Lett.*, 33, L20201, doi:10.1029/2006GL027133.

301 Fenton, L.K., Toigo A.D., Richardson, M.I. 2005. Aeolian processes in Proctor Crater on Mars:
 302 mesoscale modelling on dune-forming winds. *Journal of Geophysical Research* 110: E06005.
 303 DOI: 10.1029/2004JE002309.

304 Geissler, P.E., Stantz, N.W., Bridges, N.T., Bourke, M.C., Silvestro, S. and Fenton, L. K. 2013.
 305 Shifting sands on Mars: insights from tropical intra-crater dunes. *Earth Surf. Process.*
 306 *Landforms*, 38: 407–412. doi: 10.1002/esp.3331.

307 Greeley, R. & Iversen, J. D. 1985. *Wind as a Geological Process on Earth, Mars, Venus and Titan.*
 308 Cambridge Planetary Science Series no. 4. xii + 333 pp. Cambridge, London, New York, New
 309 Rochelle, Melbourne, Sydney: Cambridge University Press.

310 Hayward, R. K., Mullins, K. F, Fenton, L. K., Hare, T. M., Titus, T. N., Bourke, M. C., Colaprete
 311 A., Christensen. R. 2007. Mars Global Digital Dune Database and initial science results.
 312 *Journal. Of Geophysical . Research*, 112, E11007, doi:10.1029/2007JE002943.

313 Hayward, R.K., Titus, T.N., Michaels, T.I., Fenton, L.K., Colaprete, A., and Christensen, P.R.
 314 2009. Aeolian dunes as ground truth for atmospheric modeling on Mars: *Journal of Geophysical*
 315 *Research*, v. 114, E11012, doi:10.1029/2009JE003428.

316 Hansen, C.J., Bourke, M., Bridges, N.T., Byrne, S., Colon, C., Diniega, S., Dundas, C., Herkenhoff,
 317 K., McEwen, A., Mellon, M., Portyankina, G., Thomas N. 2011. Seasonal Erosion and
 318 Restoration of Mars Northern Polar Dunes. *Science* 331: 575–578, doi:
 319 10.1126/science.1197636.

320 Howard, H. D. 1977. Effect of slope on the threshold of motion and its application to orientation of
 321 wind ripples. *Geological society of American Bulletin*, 88: 853-856.

322 Kok, J.F. 2010. An improved parameterization of wind-blown sand flux on Mars that include the
 323 effect of hysteresis. *Geophysical Research Letters*, v.37, L12202, doi: 10.1029/2010GL043646.

324 Jerolmack, D.J. et al. 2012. Internal boundary layer model for the evolution of desert dune fields. *Nature*
 325 *Geoscience* 5, 206-209 (2012). doi:10.1038/ngeo1381.

326 Leprince S., Barbot S., Ayoub F. and Avouac J. P. 2007. Automatic and Precise Ortho-rectification,
 327 Coregistration, and Subpixel Correlation of Satellite Images, Application to Ground

328 Deformation Measurements, IEEE Transactions on Geoscience and Remote Sensing, Vol.45,
 329 No.6, June 2007.

330 Malin, M.C., Edgett, K.S. 2000. Sedimentary rocks of early Mars. Science, 290, 1927–
 331 1937, doi:10.1126/science.290.5498.1927, 8 December 2000.

332 Mattson, S., Kirk, R.L., Heyd, R., McEwen, A.S., Eliason, E., Hare, T., Beyer, R., Howington-
 333 Kraus, E., Okubo, C., and Herkenhoff, R.L. 2011. Release of HiRISE digital terrain models to
 334 the planetary data system: 42nd Lunar and Planetary Science Conference, The Woodlands,
 335 Texas: Lunar and Planetary Institute Contribution 1608, p. 1558.

336 Michaels, T.I., and Rafkin, S.C.R. 2008. Meteorological predictions for candidate 2007 Phoenix
 337 Mars Lander sites using the Mars Regional Atmospheric Modeling System (MRAMS): Journal
 338 of Geophysical Research, v. 113, E00A07, doi:10.1029/2007JE003013.

339 McEwen, A. S., et al. 2007. Mars Reconnaissance Orbiter's High Resolution Imaging Science
 340 Experiment (HiRISE), J. Geophys. Res., 112, E05S02, doi:10.1029/2005JE002605.

341 Parteli, E. J.R., Durán, O., Bourke, M. C., Tsoar, H., Pöschel, T., Herrmann, H. 2014. Origins of
 342 barchan dune asymmetry: Insights from numerical simulations, Aeolian Research, Volume 12,
 343 March 2014. Pages 121-133, ISSN 1875-9637, <http://dx.doi.org/10.1016/j.aeolia.2013.12.002>.

344 Pelletier, J. D. 2014. Controls on the large-scale spatial variations of dune-field properties in the
 345 barchanoid portion of White Sands dune field, New Mexico. Journal of Geophysical Research:
 346 Earth Surface. <http://dx.doi.org/10.1002/2014JF003314>.

347 Rafkin, S.C.R., Haberle, R.M., and Michaels, T.I. 2001. The Mars regional atmospheric modeling
 348 system: Model description and selected simulations: Icarus, v. 151, p. 228–256,
 349 doi:10.1006/icar.2001.6605.

350 Rubin, D.M. 2012. A unifying model for planform straightness of ripples and dunes in air and
 351 water. In: Third International Planetary Dunes Workshop: Remote Sensing and Image Analysis
 352 of Planetary Dunes. Flagstaff, Arizona, abst. #7020.

353 Silvestro, S., Vaz, D.A., Fenton, L.K., Geissler P.E. 2011. Active eolian processes on Mars: A
354 regional study in Arabia and Meridiani Terrae. *G. Res. Lett.*, 38, L20201, doi:
355 10.1029/2011GL048955.

356 Silvestro, S., Fenton, L. K., Michaels, T. I., Valdez, A. and Ori, G. G. 2012. Interpretation of the
357 complex dune morphology on Mars: dune activity, modelling and a terrestrial analogue. *Earth*
358 *Surf. Process. Landforms*, 37: 1424–1436. doi: 10.1002/esp.3286

359 Silvestro, S., Vaz, D. A., Ewing, R.C., Rossi, A.P., Fenton, L.K., Michaels, T.I., Flahaut J., and
360 Geissler, P.E. 2013. Pervasive aeolian activity along rover Curiosity’s traverse in Gale Crater,
361 Mars. *Geology*, 2013, doi:10.1130/G34162.1.

362 Sparavigna, Amelia Carolina. 2013. Edge-detection applied to moving sand dunes on Mars. *arXiv*
363 *preprint arXiv:1308.5315*.

364 Vaz, D.A., Silvestro, S. 2012. An object based approach for the mapping and characterization of
365 Mars ripples. In: *The Third International Planetary Dunes Workshop: Remote Sensing and*
366 *Image Analysis of Planetary Dunes*, Vol. Abs #7019, Flagstaff, AZ, USA.

367 Vaz, D.A., Silvestro S. 2014. Mapping and characterization of small-scale aeolian structures on
368 Mars: An example from the MSL landing site in Gale Crater. *Icarus*, Volume 230, 15 February
369 2014, Pages 151-161. Third Planetary Dunes Systems.
370 <http://dx.doi.org/10.1016/j.icarus.2013.08.007>.

371

372

373 **Supplemental table**

- 374 1. S1-S2-T3 HiRISE acquisition parameters.
- 375 2. Statistical parameters of the modeled winds divided by seasons.

376

377 **Captions**

- 378 1. a) Details of the study area, showing the distribution of the large dark dune fields within

Herschel Crater (MOLA shaded topography with Themis daytime mosaic). **b)** A perspective view of the large dark dunes from HiRISE images PSP_002860_1650 and ESP_020384_1650. A shaded relief map from MOLA data (top), showing the location of Herschel Crater.

- 2.** The Herschel Crater dune field (CTX image P05_002860_1650_XI_15S232W) slope map derived from High Resolution Imaging Science Experiment digital terrain models (DTMs). **b-c)** Barchan dunes with and without elongated horns in the northern and north-eastern area of the dune field. The slope map suggests the presence of a slipface with a trend of 62° - 286° , denoting a predominant wind direction blowing from the northeast (HiRISE image PSP_002860_1650). **d)** The lower hemisphere equal-area density stereoplot for all the slipface surface vectors estimated from the HiRISE DTMs. The estimated dip angle is $\sim 30^{\circ}$
- 3. a)** This inset represents the ripple length-weighted circular distribution (the mapped area corresponds to the yellow window shown in Fig. 2). The mapped ripple population exhibits a bimodal trend with two main modes trending 45° and 135° . **b)** An inset of a horn of a dune, where along its flanks, the ripple crests are continuous and have a two dimensional pattern. **c)** The pattern of the ripples superposing the dune's slopes is complex due to the diverse wind flows blowing over the dunes.
- 4. a)** Average dune lee front migration vectors overlain on the DTM. The colored vectors represent the average displacement of the slipface lee fronts over three Earth-years (from March 2007 to December 2010). **b-c)** The plots represent the statistics computed using 500 m moving windows for the migration and elevation at the base of the slipfaces. Note the general decrease of the displacements when moving south, and the association of the area with larger migrations (between -14.7° and -14.75°) with a drop in elevation.
- 5. a)** This rose diagram shows the distribution of lee side migration azimuth. **b)** This rose diagram shows the circular distribution of the lee side migration.
- 6.** Ripple displacement map for the Herschel Crater dune field, derived from correlated

HiRISE images with high displacements shown with warmer colors. **b)** Fast ripples moved so much that the correlation breaks down causing the observed fuzzy pattern. **c)** Area in which the correlation starts to record the ripple migration.

7. Circular distribution of the migration vectors. **a)** Ripple migration mean vector. **b)** This rose diagram shows the circular distribution of all ripple migration vectors. The secondary mode at $\sim 240^\circ$ is due to the ripple migration vectors in the lee of the dunes (see Figure 8).

8. Daily maximum MRAMS stress (ratio) vectors computed from COSI-Corr vectors data.

9. MRAMS modeled wind stresses and directions. **a)** Daily maximum stress ratio vectors for each of the 36 model nodes covering the dune field. The azimuth of the vectors corresponds to the wind direction while the color is the ratio between the model aerodynamic surface stress and the aerodynamic stress threshold for saltation initiation (Greeley and Iversen, 1985) **b)** Circular standard deviation associated with the mean vectors shown in a). **c)** Circular distribution of the wind stress ratio vectors. **d)** Mean stress ratio vectors of the modeled winds divided by seasons.

10. MRAMS winds in a GIS format over the studied dune field during the 12 investigated seasons. Only winds $>10\%$ of the Greeley and Iversen saltation initiation threshold are included in this plot. Each vector shows the downwind direction of the wind (the direction of the wind is flowing toward). The length of each vector is proportional to the greatest $\text{sfc_stress}/\text{sfc_stress_threshold}$ ratio at the point of the direction while the color shows the relative frequency of each wind direction at each point (warmer colors correspond to more winds blowing in that direction).

11. Each circular distribution contains the combined information of all 21 MRAMS higher resolution points within the outline of one of the studied HiRISE images (see Fig.10). The radial direction in these plots is magnitude (of $\text{stress}/\text{stress_threshold}$), with the outer ring being a value of 0.3 and the center of each plot being 0. Each bin is colored by the relative frequency of each wind direction/magnitude (warmer colors correspond to more winds

431 blowing in that direction).

432 **12.** The circular distribution shows the sum of all the 12 investigated seasons.

Table1
[Click here to download high resolution image](#)

	<i>S1</i>	<i>S2</i>	<i>T3</i>
Product ID	PSP_002860_1650	PSP_003572_1650	ESP_020384_1650
Acquisition Date	07 March 2007	01 May 2007	01 Dicember 2010
Resolution	0.25m/pixel	0.25m/pixel	0.25m/pixel
Latitude (centered)	-14.807 degrees	-14.805 degrees	-14.813 degrees
Longitude (est)	127.888 degrees	127.890 degrees	127.897 degrees
Local Mars time	3.44 PM	3.22 PM	3.41 PM
Solar longitude	195.9 degrees, Northern Autumn	229.7 degrees, Northern Autumn	190.9 degrees, Northern Autumn
Solar incidence angle	56 degrees	49 degrees	55 degrees
Sub solar azimuth	7.3 degrees	351.4 degrees	9.7 degrees
Emission angle	2.4 degrees	27.3 degrees	4.5 degrees

<i>STRESS RATIO</i>			
Solar Longitude (°)	Mean Azimuth (°)	Mean Stress Ratio (°)	Circular Standard Deviation
30	88,72726	0,03521729	33,93312
120	67,86047	0,005481146	86,73132
210	145,4258	0,005119130	103,0098
300	232,3831	0,003217317	120,6203

Figure1

[Click here to download high resolution image](#)

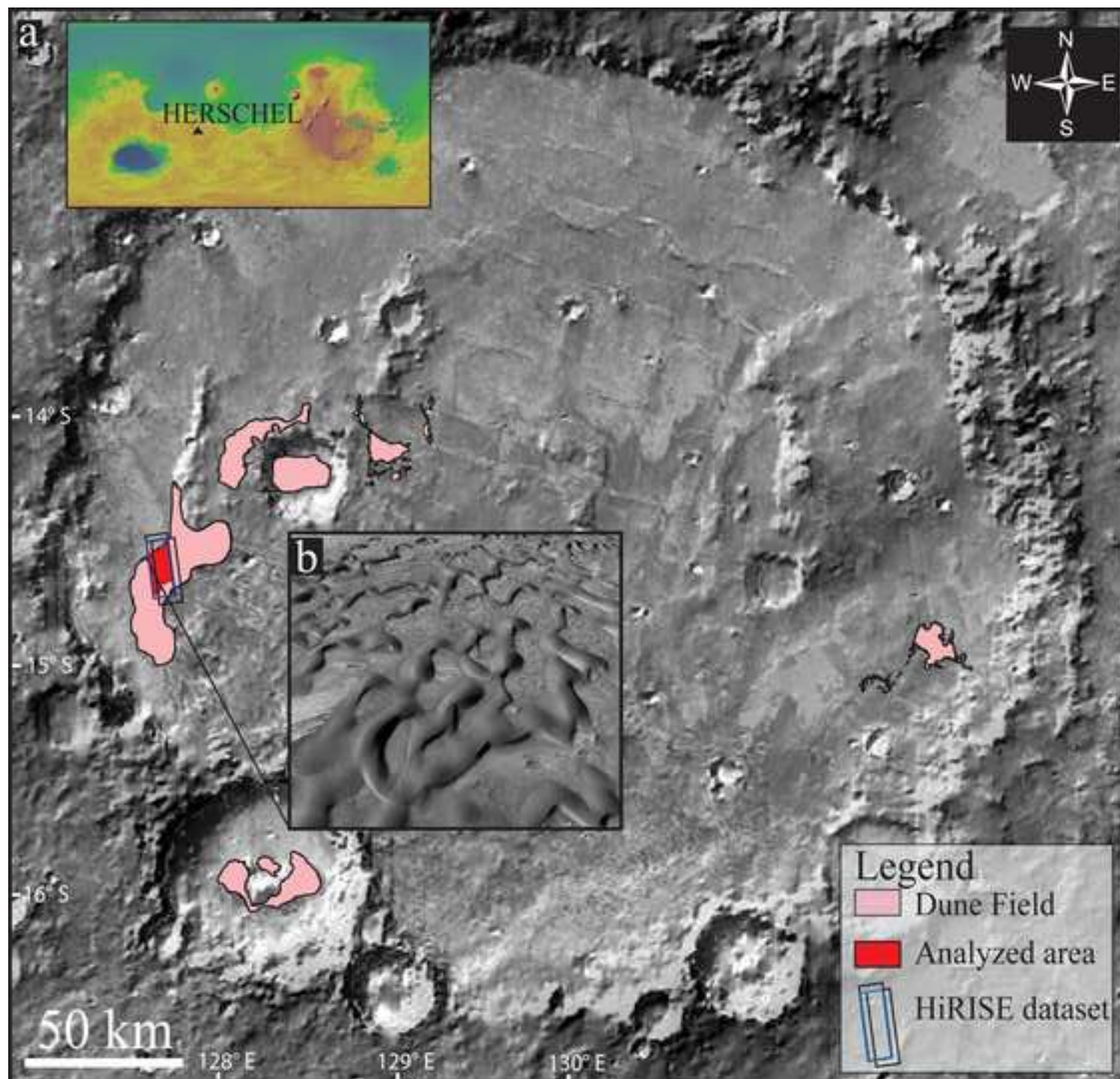


Figure2
[Click here to download high resolution image](#)

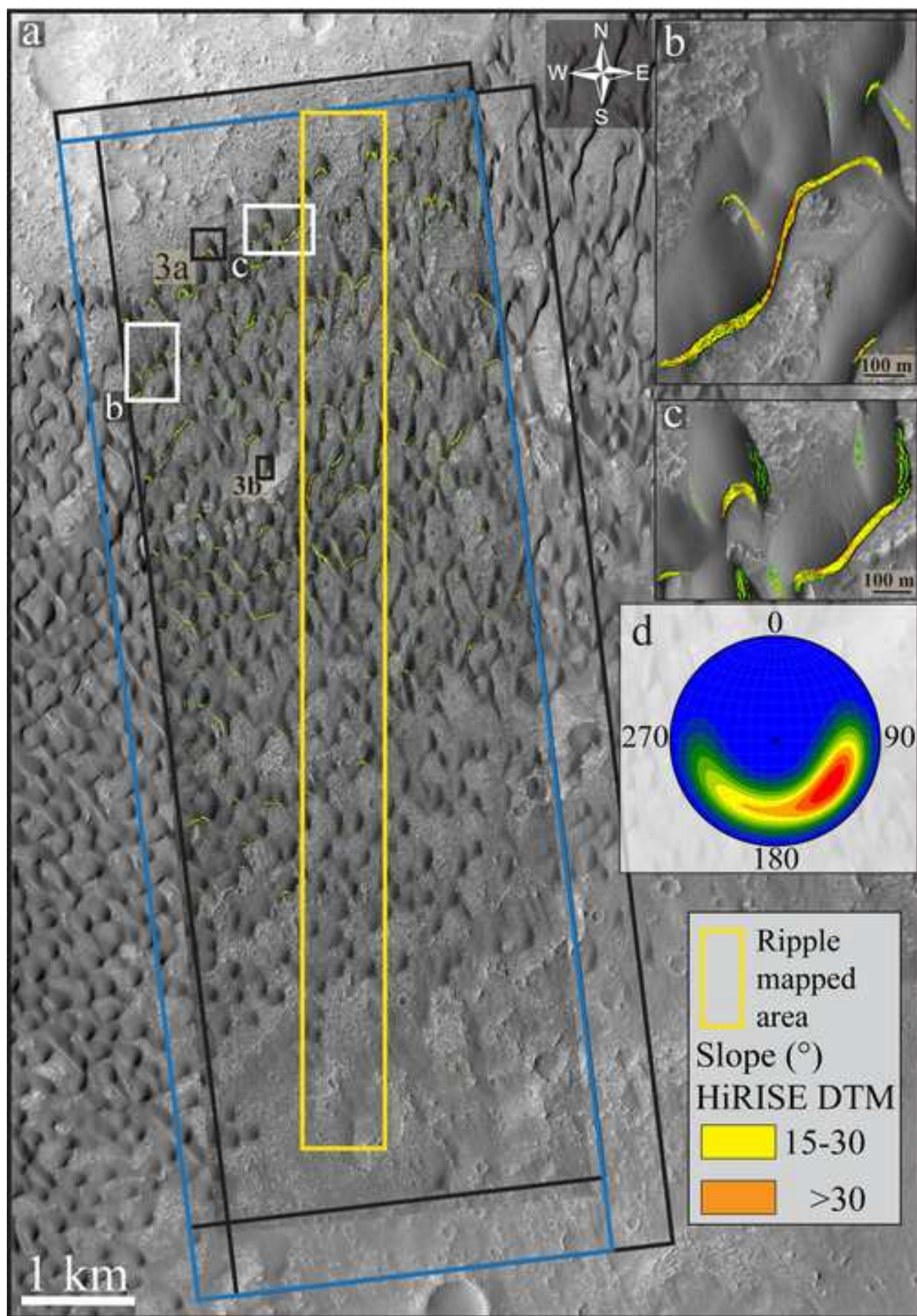


Figure3
[Click here to download high resolution image](#)

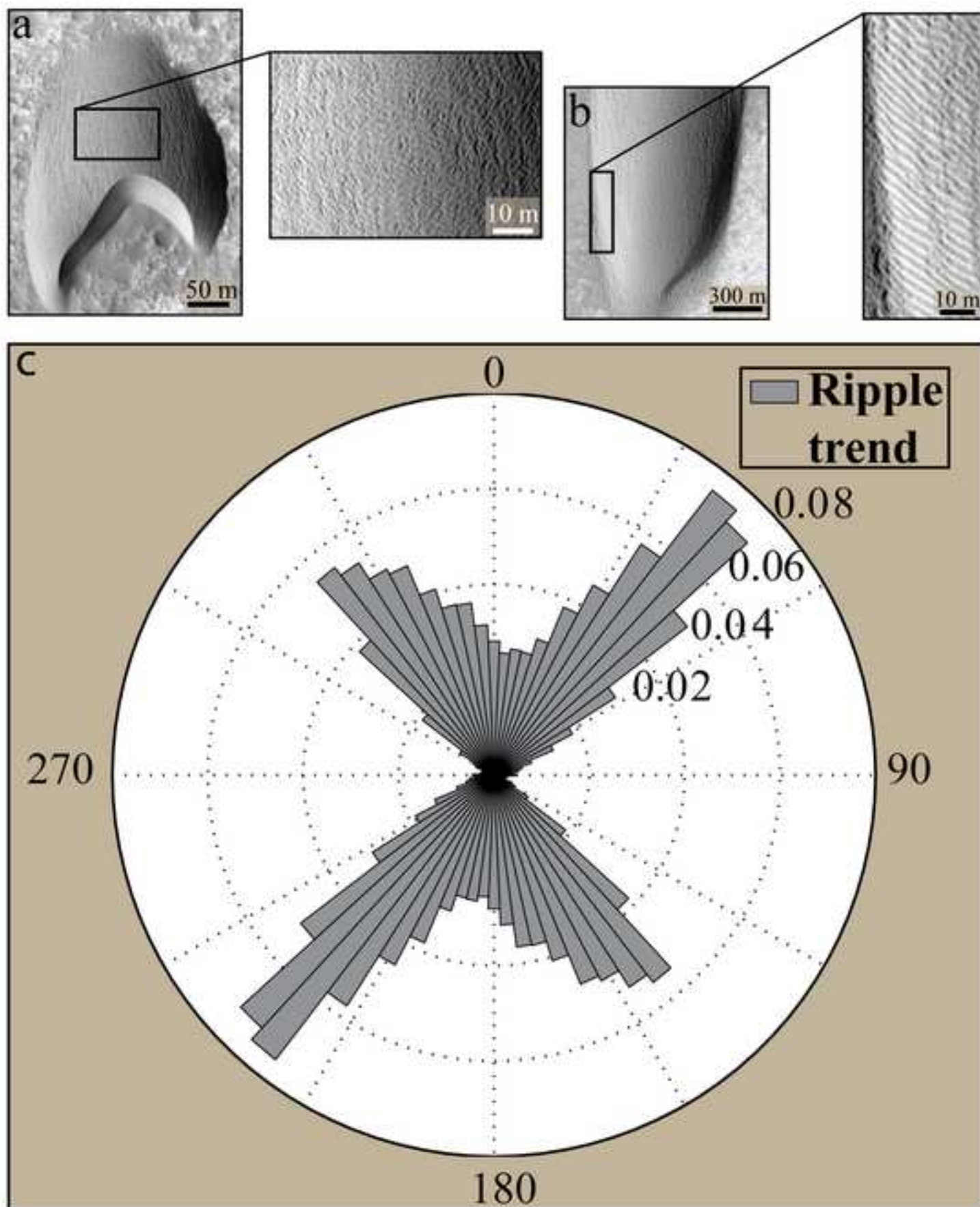


Figure4
[Click here to download high resolution image](#)

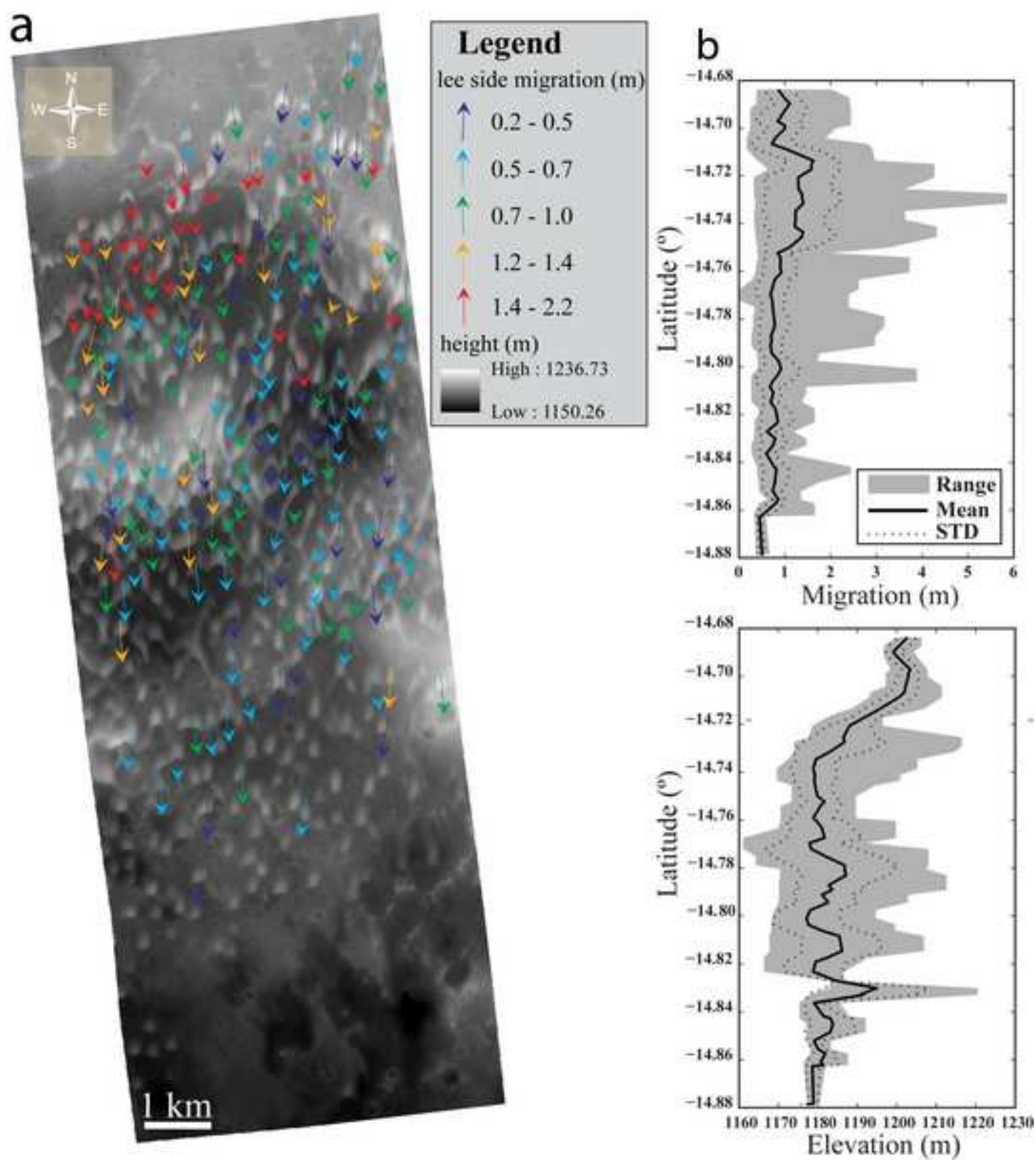


Figure5

[Click here to download high resolution image](#)

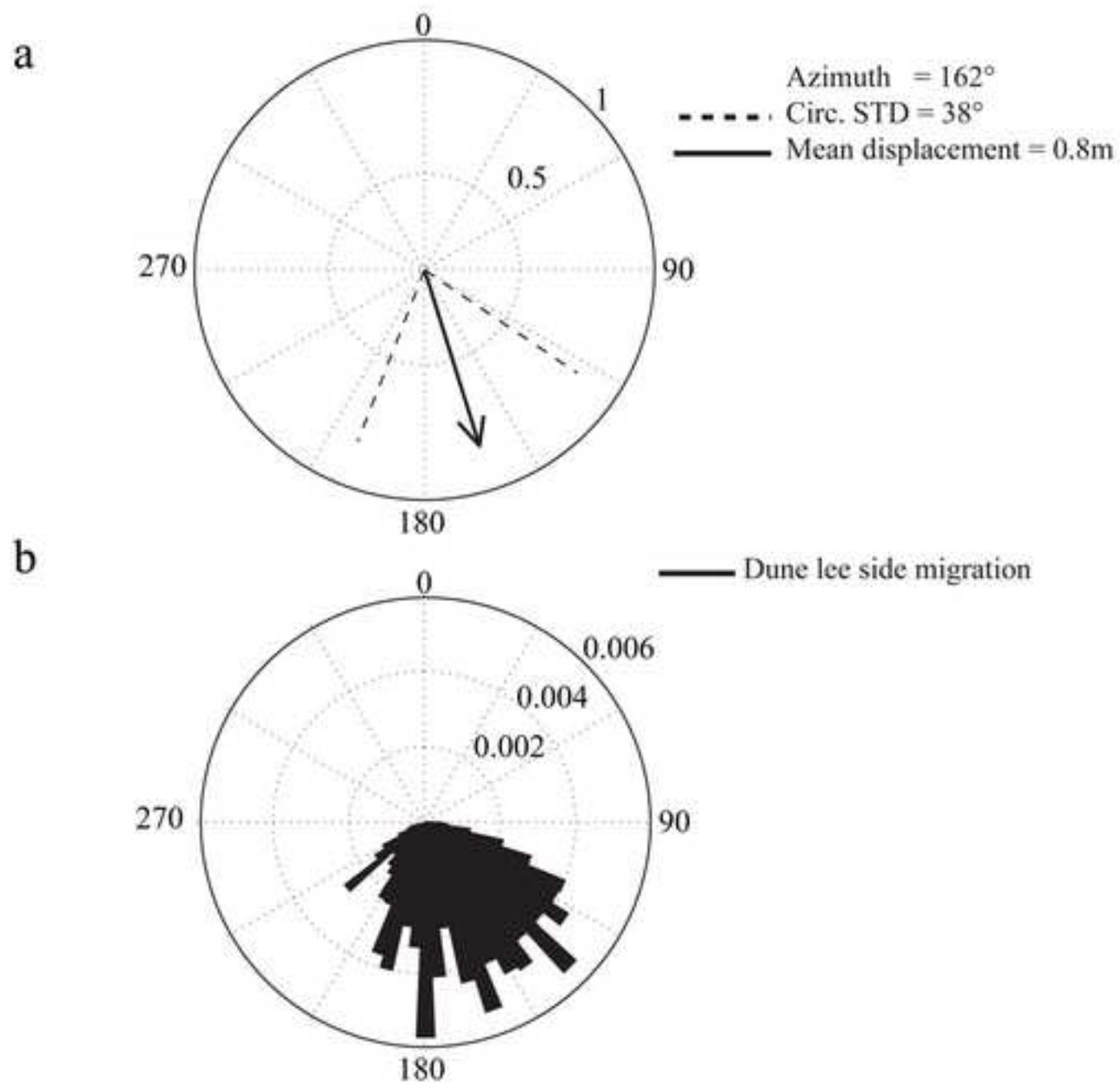


Figure6
[Click here to download high resolution image](#)

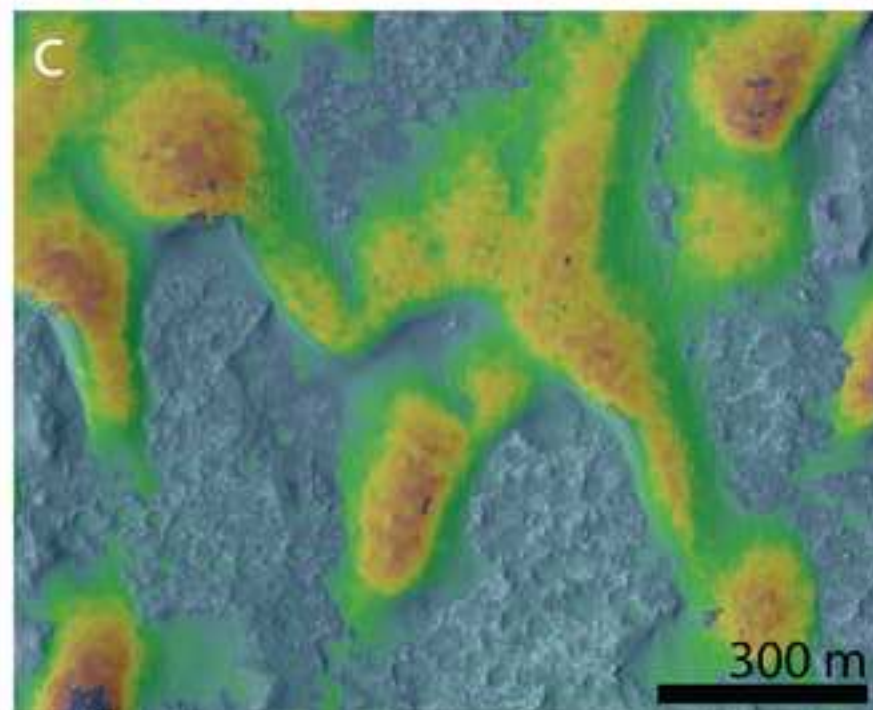
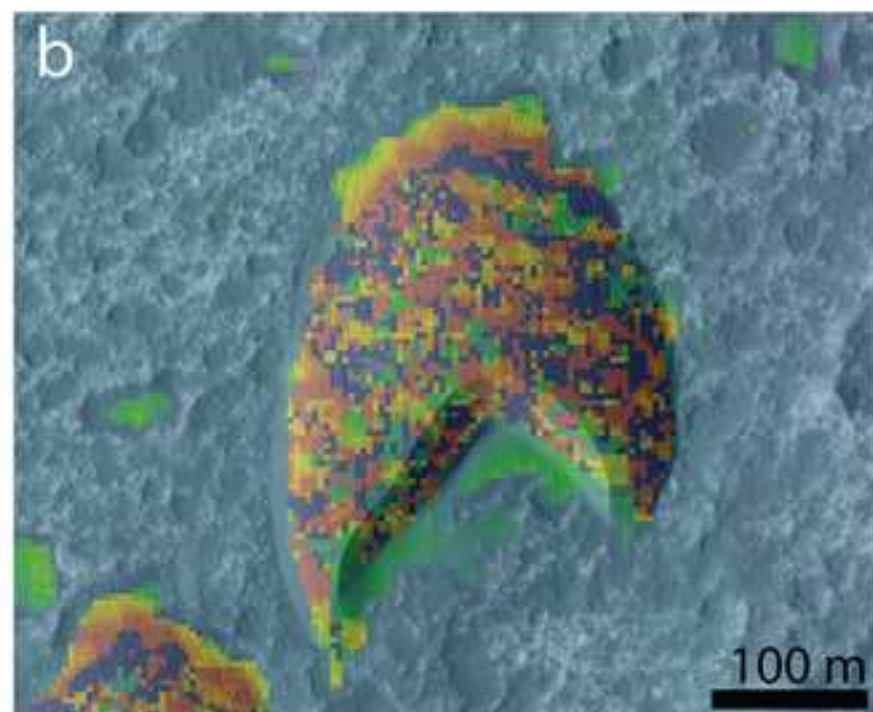
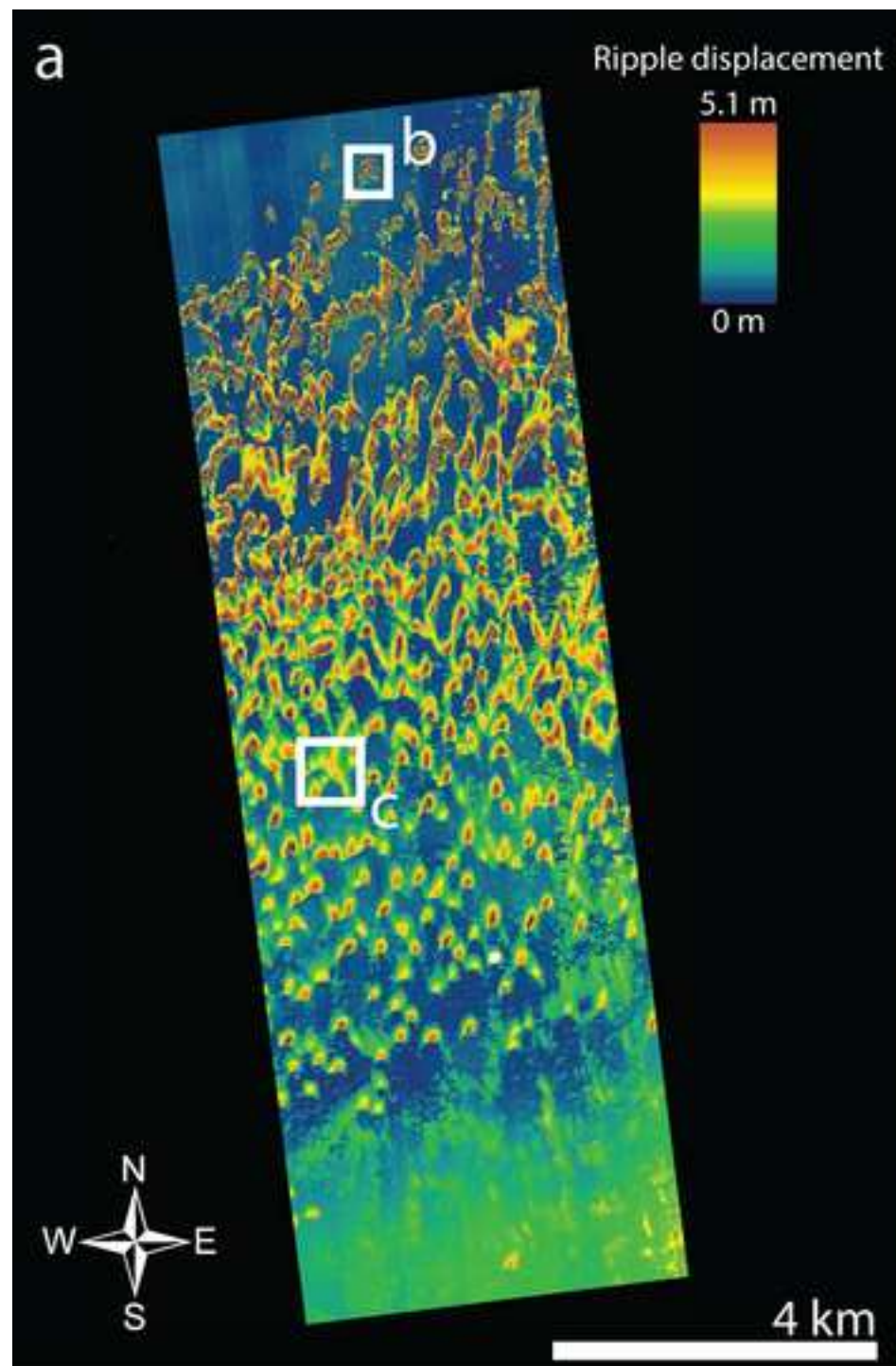


Figure7
[Click here to download high resolution image](#)

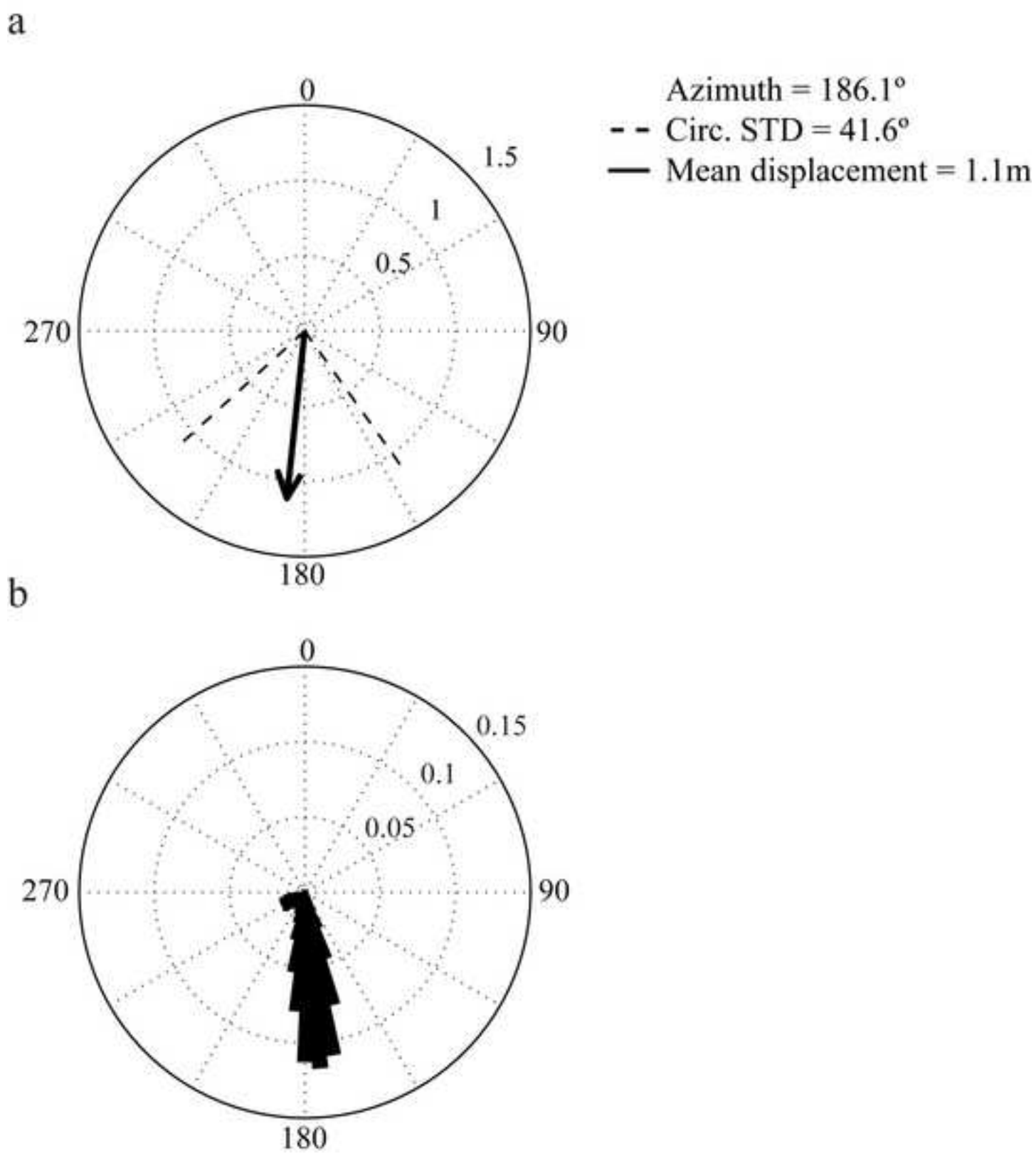


Figure8
[Click here to download high resolution image](#)

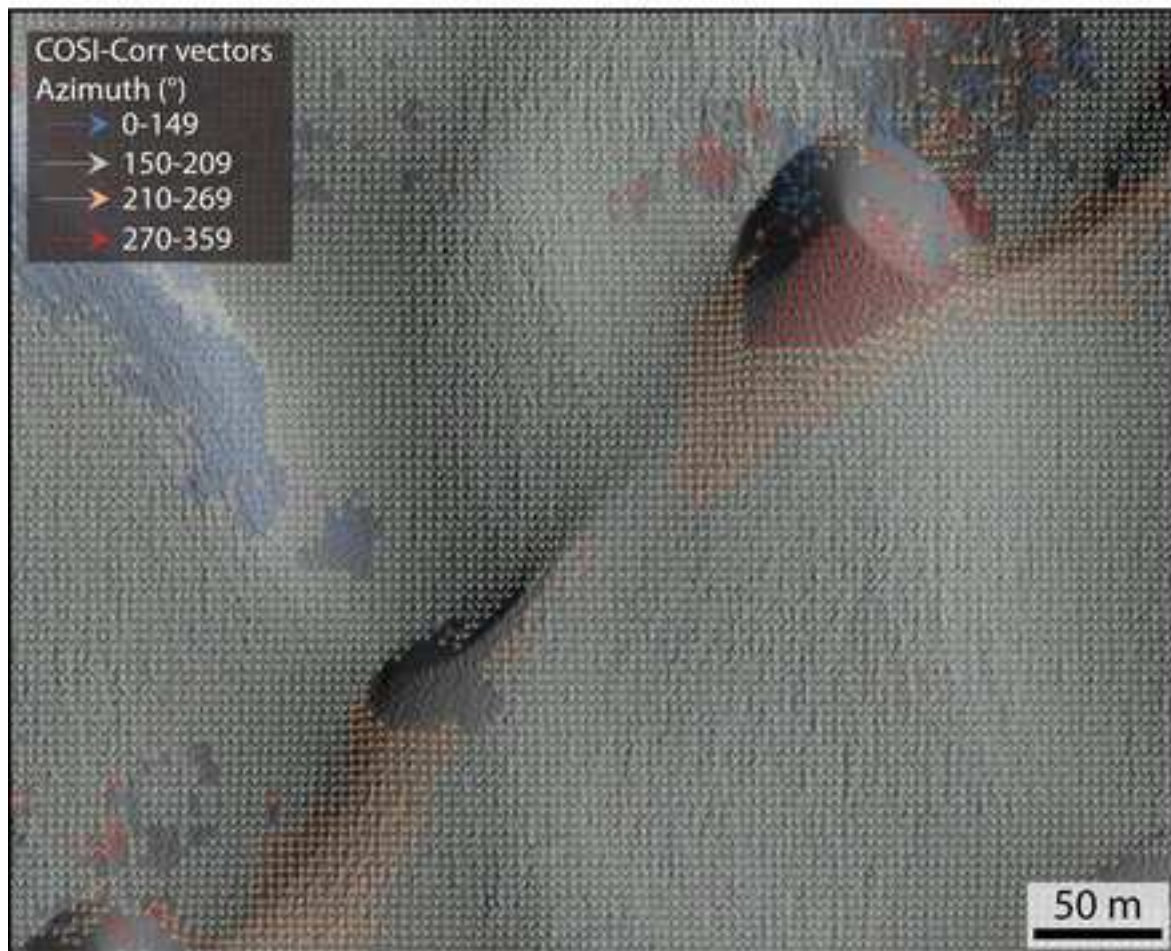
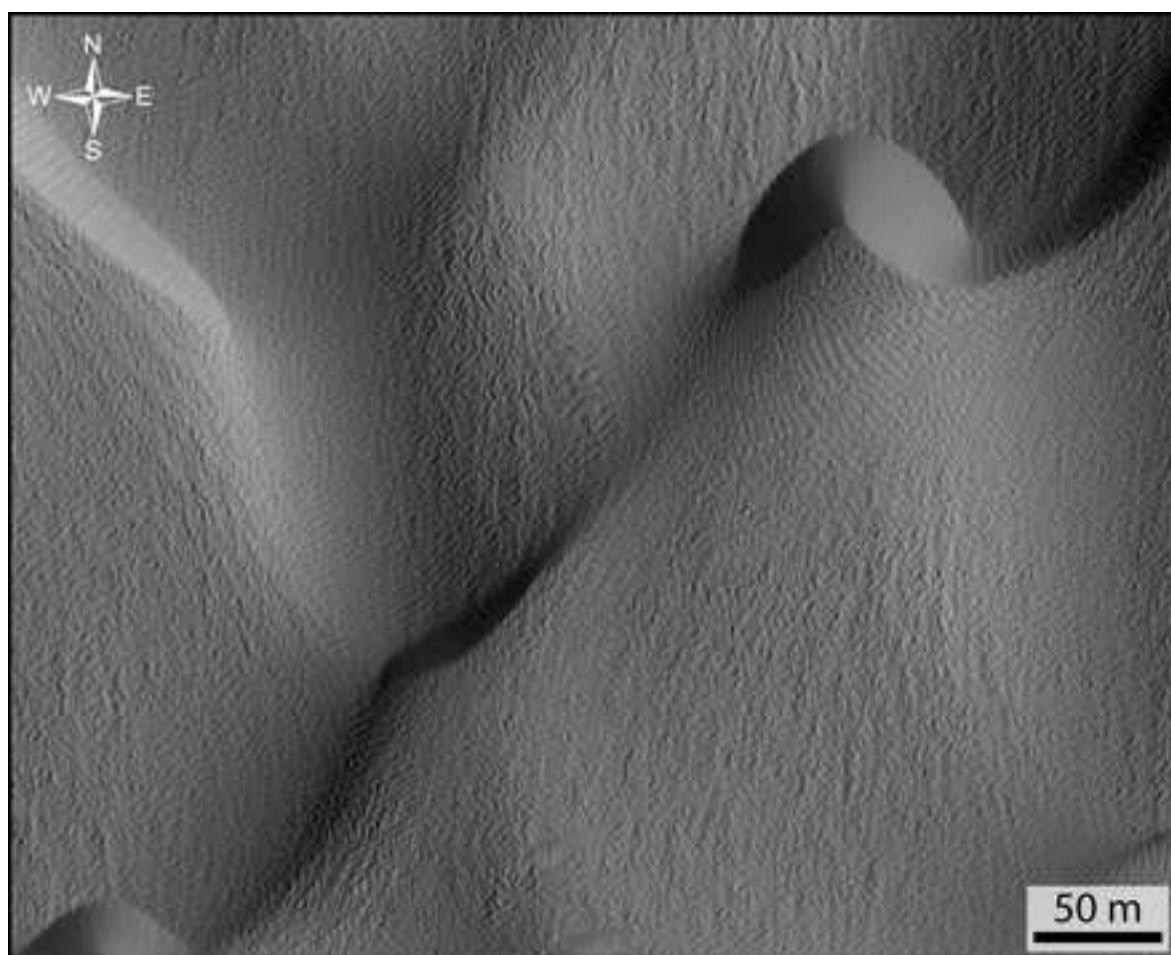
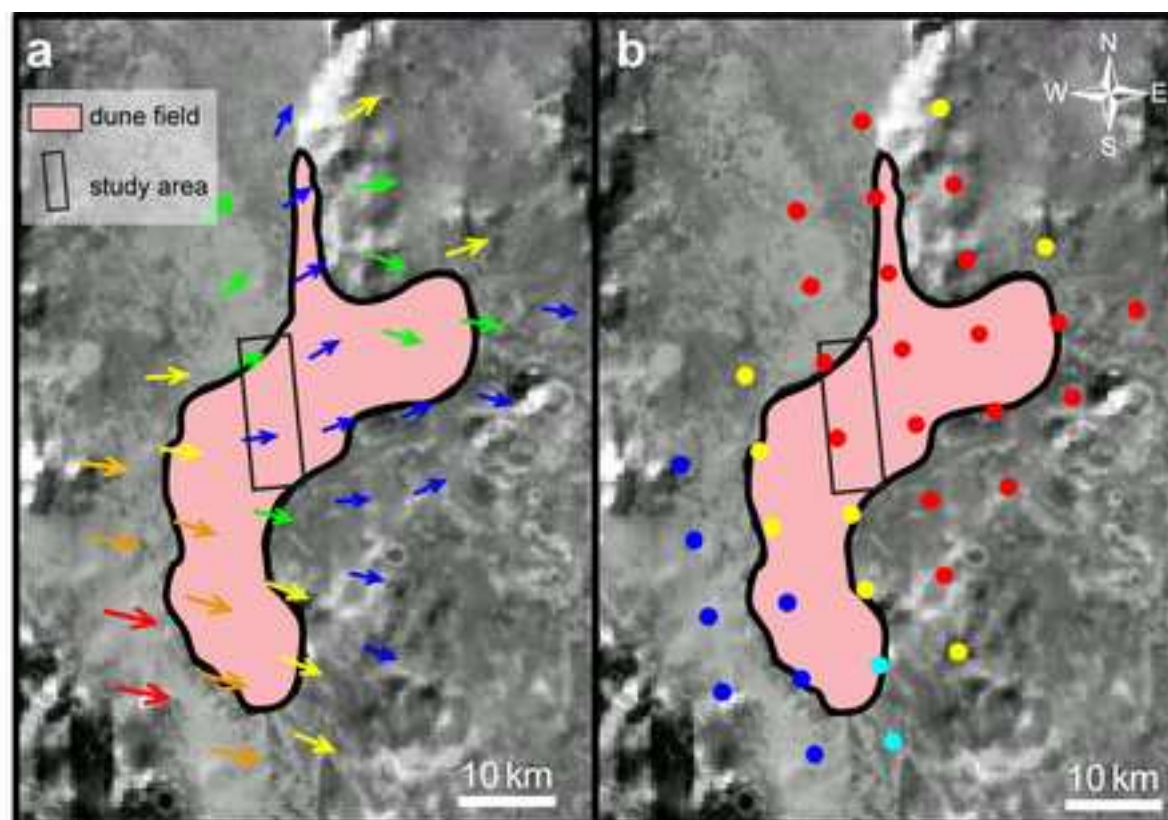
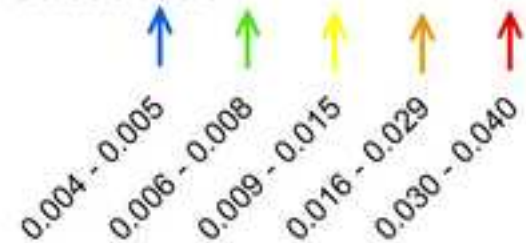


Figure9
[Click here to download high resolution image](#)



MRAMS

Stress ratio



Circ. st. dev (°)

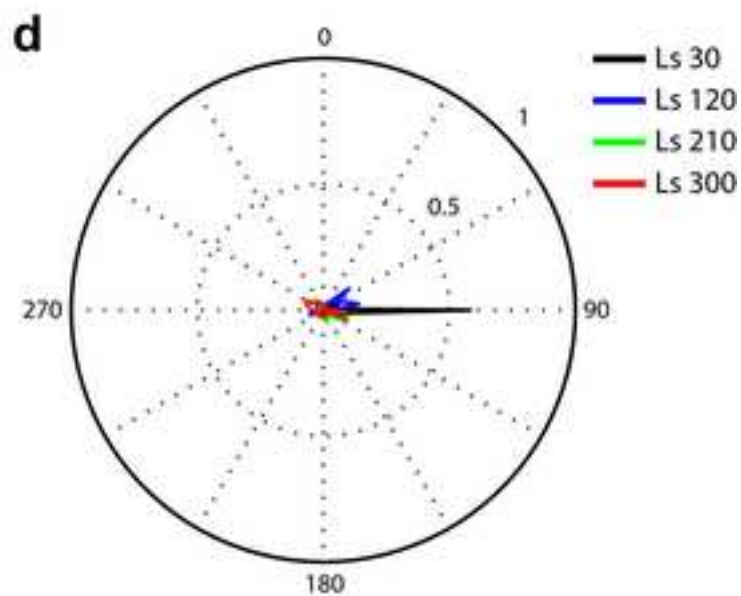
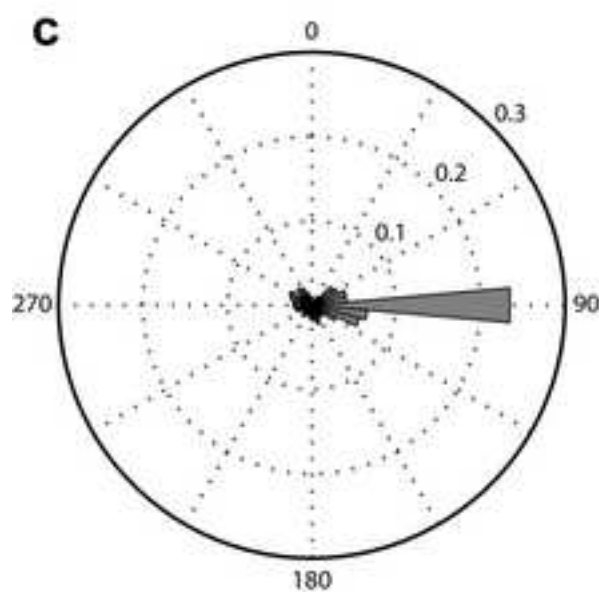
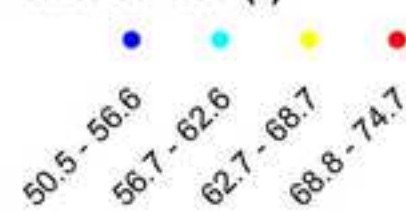


Figure10
[Click here to download high resolution image](#)

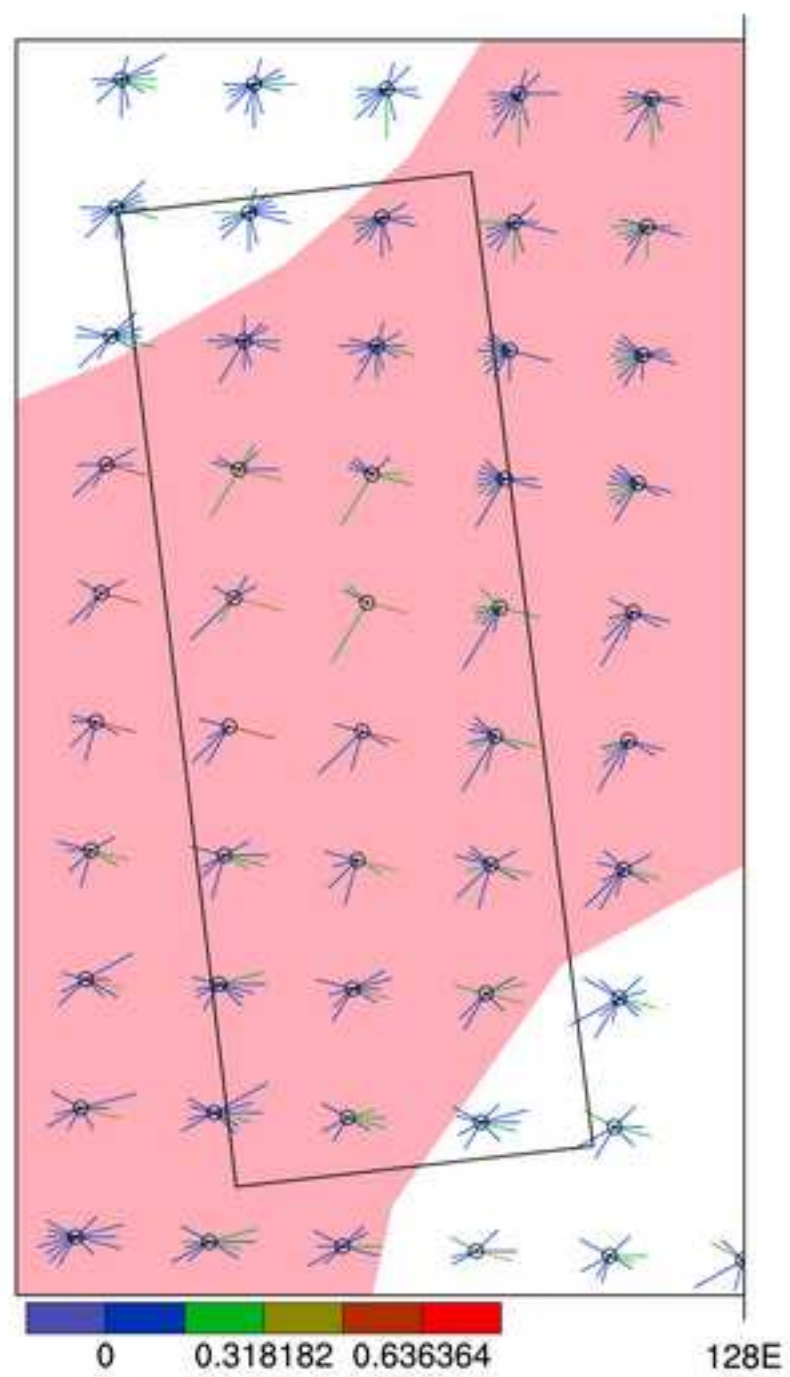


Figure11
[Click here to download high resolution image](#)

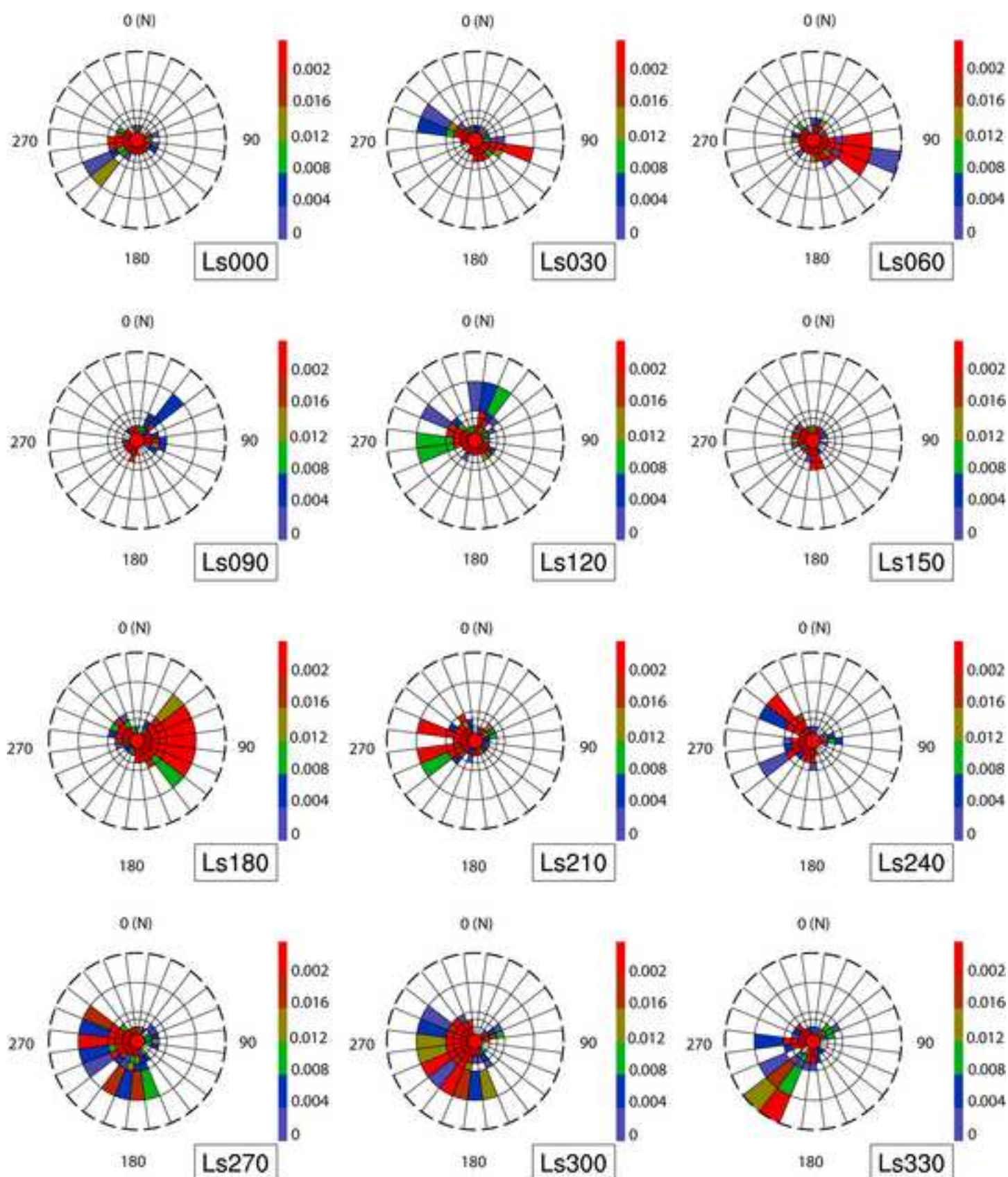


Figure12

[Click here to download high resolution image](#)

